

# Compositional 3D Scene Synthesis with Scene Graph Guided Layout-Shape Generation

Yao Wei<sup>1</sup>, Martin Renqiang Min<sup>2</sup>, George Vosselman<sup>1</sup>, Li Erran Li<sup>\*3</sup>, and Michael Ying Yang<sup>4</sup>

<sup>1</sup>University of Twente, The Netherlands {yao.wei, george.vosselman}@utwente.nl

<sup>2</sup>NEC Laboratories America, USA renqiang@nec-labs.com

<sup>3</sup>AWS AI, Amazon, USA erranli@gmail.com

<sup>4</sup>University of Bath, UK myy35@bath.ac.uk

## Abstract

*Compositional 3D scene synthesis has diverse applications across a spectrum of industries such as robotics, films, and video games, as it closely mirrors the complexity of real-world multi-object environments. Early works typically employ shape retrieval based frameworks which naturally suffer from limited shape diversity. Recent progresses have been made in shape generation with powerful generative models, such as diffusion models, which increases the shape fidelity. However, these approaches separately treat 3D shape generation and layout generation. The synthesized scenes are usually hampered by layout collision, which implies that the scene-level fidelity is still under-explored. In this paper, we aim at generating realistic and reasonable 3D scenes from scene graph. To enrich the representation capability of the given scene graph inputs, large language model is utilized to explicitly aggregate the global graph features with local relationship features. With a unified graph convolution network (GCN), graph features are extracted from scene graphs updated via joint layout-shape distribution. During scene generation, an IoU-based regularization loss is introduced to constrain the predicted 3D layouts. Benchmarked on the SG-FRONT dataset, our method achieves better 3D scene synthesis, especially in terms of scene-level fidelity. The source code will be released after publication.*

## 1. Introduction

Generative models [15, 11, 29, 13] have shown great potential in computer vision, natural language processing and multi-modal learning. With the learned patterns from

generative models, data can be synthesized from scratch or other modalities. For controllable content creation, which has attracted increasing attention from both academia and industry, a variety of conditional generative methods have emerged on tasks such as text-to-image [27, 31], image-to-3D [19, 18] and text-to-3D [14, 32] generation. These cross-modal synthesis methods significantly reduce the data acquisition budget, especially for 3D content whose collection requires a lot of human efforts.

Despite the recent impressive breakthroughs in 3D content creation, most of the existing works [39, 20, 35, 4] are restricted to single-object scenes, and their performance inevitably degrades on compositional scenes due to the limited understanding of object-object and scene-object relationships. Even trained on Internet-scale captioned 3D objects, for instance, Shap-E [14] struggles to reliably produce the results that are consistent with the given spatial or numerical prompts. Moreover, labor-intensive post-processing is essential to scale these approaches to complex scenes containing multiple objects, since the synthesized 3D shapes are sometimes in the non-canonical space.

In recent years, new pipelines capable of producing the entire 3D scenes have been developed using diverse inputs, such as LiDAR scans [28], single RGB images [8], captioned bounding boxes (i.e., scene layouts) [25] and scene graphs [22, 7, 38]. As a semantic representation of 3D scenes, scene graphs provide a promising interface to control the generated 3D content, e.g., assigning properties to different instances of the same object category. However, 3D scene synthesis from scene graph is still at an early stage, and existing methods encounter various challenges.

Conventional works focus on scene layout generation regardless of 3D shape generation. Instead, the object shapes are retrieved from the existing shape databases. Though benefiting from good shape quality, as illustrated in Fig. 1

\*Work done outside of Amazon.

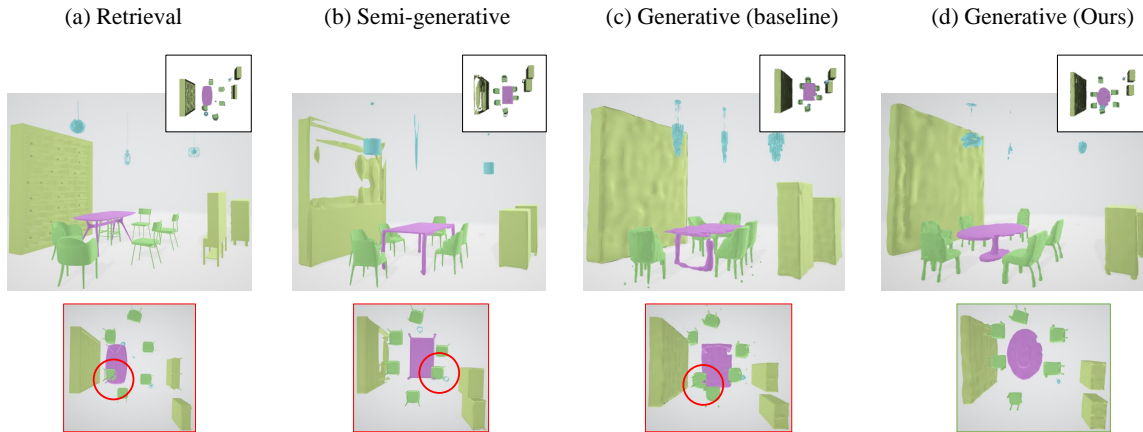


Figure 1. Overview of previous works and ours. The 3D scenes are rendered from top-down view (top right), side view (middle), and bottom-up view (bottom). Unlike previous works that show poor shape consistency or spatial arrangements, our method can synthesize higher-fidelity 3D scenes which demonstrate more realistic layout configuration while preserving shape consistency and diversity.

(a), it is hard for retrieval-based methods to generate coherent 3D scenes. For example, chairs appear in arbitrary shape styles. In addition, the performance heavily depends on the scale of the given databases. Differently, recent works synthesize the 3D scenes from semi- or fully-generative perspectives. By category-specified shape decoders, semi-generative method Graph-to-3D [7] alleviates the limitation of retrieval-based method on shape consistency, but it suffers from low-quality shapes such as the incomplete wine cabinet shown in Fig. 1 (b). Fully-generative method CommonScenes [38] enables shape generation by adopting a latent diffusion model, which enhances the shape fidelity and diversity. Nevertheless, it can be seen from Fig. 1 (c) that the generated objects are spatially ambiguous due to the poor scene layouts. In fact, this is common in (a), (b) and (c) where the table intersects the adjacent chair, denoted with red circles in bottom-up views. These unrealistic generations leave a huge gap between previous methods and practical applications.

For controllable 3D scene synthesis, the generated objects should be not only realistic on its own but in harmony with the context of scene. To this end, we present a new approach for scene graph guided 3D scene synthesis. Instead of treating the compositional scene synthesis as two separate tasks, we work on joint layout-shape generation. For encoding stage, scene graphs are updated with aggregated features, which are then extracted by a unified graph convolution network (GCN) to enable communication between 3D shape modeling and spatial arrangements. Furthermore, a layout regularization loss is introduced to encourage reasonable arrangements. As illustrated in Fig. 1 (d), our method is capable of generating realistic compositional 3D scenes. The **contributions** made in this work can be summarized as follows.

- Through joint learning of 3D layout-shape generation conditioned on scene graphs, a novel end-to-end method is proposed for compositional 3D scene synthesis.
- LLM enhances the graph representation by interpreting the whole graph, which enables better understanding of object-object and scene-object relationships.
- A layout regularization loss is introduced to generate reasonable spatial arrangements.
- The experimental results demonstrate that our method can achieve better 3D scene synthesis. Compared to the state-of-the-art CommonScenes [38], our method has reached 2.55 lower Fréchet Inception Distance (FID) score and 1.24 lower Kernel Inception Distance (KID) score.

## 2. Related Work

Unlike object-centric synthesis, compositional 3D scene synthesis is a challenging problem where the object attributes and relationships both play a role. For simplification, prior works [22, 8, 25, 28, 7, 38] usually characterize a scene by spatial layouts and 3D shapes of the objects-of-interest within the scene. These works can be broadly divided into three types of solutions. We also survey emerging large language models which are relevant to our work.

**Shape retrieval based methods.** Early works [22, 8] formulate the scene synthesis task as a combination of 3D layout prediction problem and 3D shape selection problem. They present two-stage approaches where 3D layouts are estimated from the input conditions and category-aware 3D shapes are then selected or retrieved from the given

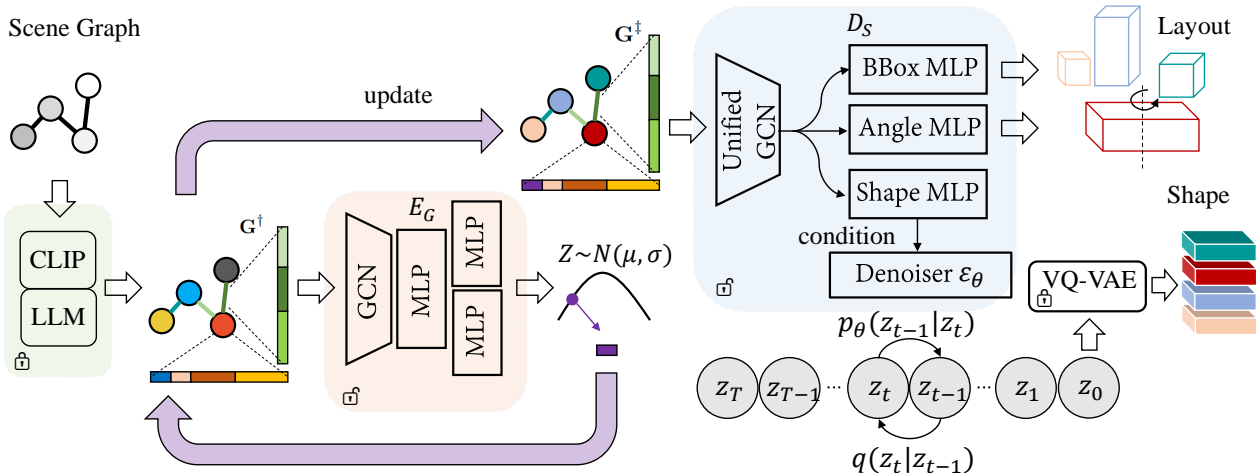


Figure 2. Overall pipeline for training phase. The proposed method consists of a scene graph encoder  $E_G$  and a 3D scene decoder  $D_S$ . First, we enrich the scene graph representation with CLIP and LLM, which explicitly aggregates object-wise, relationship-wise and graph-wise text descriptions.  $E_G$  learns to model a joint layout-shape distribution  $Z$  which is utilized for updating the node features of scene graphs. Besides, a unified GCN extracts graph features which are then feed with three MLP modules: BBox MLP for 6-parameterized layout prediction, Angle MLP for rotation prediction, and Shape MLP for deriving shape code that conditions the denoising diffusion model for shape generation. Finally, 3D scenes can be synthesized by fitting the 3D shapes reconstructed from VQ-VAE decoder to the generated layouts.

databases such as ShapeNet [3]. However, this formulation depends on the scale of the databases and suffers from limited diversity in 3D shapes.

**Semi-generative models.** Given axis-aligned bounding boxes with corresponding text prompts, Comp3D [25] is able to synthesize compositional 3D scenes that fit the input specifications. While benefiting from Neural Radiance Fields (NeRF) [23] and extensive 2D image data, the 3D generation usually demonstrate the Janus face problems. With real 3D shape representations, XCube [28] can produce high-quality meshes conditioned on LiDAR point clouds capturing driving scenarios. However, these partial observations are obviously not user-friendly inputs. Graph-to-3D [7] is a pioneering work in jointly generating 3D shapes and layouts from scene graphs, which overcomes the former limitations. However, this semi-generative based solution is bounded by pre-trained category-wise shape decoders.

**Fully-generative models.** By replacing the pre-trained shape decoders with latent diffusion, a fully-generative method CommonScenes [38] is recently proposed for scene graph-to-3D scene synthesis in an end-to-end manner. However, the inferred 3D scenes usually suffer from issues such as object collisions, leading to unrealistic generation.

**Annotations generated by large language model.** High quality labels in natural language play a vital role for machine learning (ML) systems. Traditionally, they are collected from humans manually or with limited ML assis-

tance. Due to the high cost, large datasets with high quality text annotations are rare which hampers progress in the field. Recently, as large language models (LLMs) such as GPT-4 are very capable, prior work has successfully employed LLMs to automatically generate annotations. In the NLP domain, besides earlier successes on generate annotations for tasks such as relevance detection, topic classification, and sentiment analysis, recently [24] shows GPT-4 can even generate data to solve advanced reasoning tasks. In the realm of images, LLMs are widely employed to generate question-answer text pairs from image captions for instruction tuning [17, 2, 40]. In video datasets, LLMs are primarily employed to enrich the text descriptions of videos. For instance, MAXI [34] leverages LLMs to generate additional textual descriptions of videos from their category names for training. InternVideo [36] utilizes LLMs to generate the action-level descriptions of videos from their frame-level captions. HowtoCap [16] leveraged LLMs to enhance the detail in narrations of instructional videos. By contrast, we employ LLMs to generate global descriptions of the scene graph. These rich and consistent descriptions prove to be vital to improve the representation learning in order to generate realistic scenes.

### 3. Method

Given a scene graph describing the 3D scene by object categories and relationships, our method aims to synthesize the desired compositional 3D scene which can be characterized by 3D layouts and 3D shapes. As shown in Fig. 2,

an encoder-decoder framework is adopted in our work. We first leverage a graph encoder  $E_G$  to model the posterior distribution of the 3D scene conditioned on the given scene graph. Then, a scene decoder  $D_S$  learns to generate scenes using layout branch and shape branch.

### 3.1. Scene Graph Representation

A scene graph  $\mathbf{G} = (O, R)$  consists of objects  $O = \{o_1, o_2, \dots, o_N\}$  (i.e.,  $N$  nodes) and relationships  $R = \{r_1, r_2, \dots, r_M\}$  (i.e.,  $M$  directed edges) between objects. The representation of scene graph is initially composed of a set of node features  $\mathcal{F}_O \in \mathbb{R}^{N \times Q}$  and edge features  $\mathcal{F}_R \in \mathbb{R}^{M \times 2Q}$ , embedded from the classes of objects  $O$  and relationships  $R$ , respectively.  $Q$  indicates the dimensions of feature vectors. Then, we concatenate  $\mathcal{F}_O$  with layout features  $\mathcal{F}_B \in \mathbb{R}^{N \times Q}$  which are embedded using ground-truth 7-degrees-of-freedom layouts of 3D objects, yielding  $\mathcal{F}_O^B \in \mathbb{R}^{N \times 2Q}$ .

To enrich  $\mathcal{F}_O^B$  and  $\mathcal{F}_R$  with inter-object insights, a contextual graph [38] is constructed by employing the pre-trained and frozen text encoder from the visual-language model CLIP [26]. Taking the relationship triplets  $\langle \text{subject}, \text{predicate}, \text{object} \rangle$  as text prompts, the text encoder produces contextual features  $\mathcal{F}_R^C$  for edges. Meanwhile, CLIP-based node features  $\mathcal{F}_O^C$  are derived with prompts on subjects and objects of relationship triplets. Furthermore, we adopt a pre-trained and frozen large language model Instructor Transformer [30] to further enhance the expressiveness of scene graph. With the instruction "Represent the Science document for summarization", Instructor extracts the textual features from aggregated relationship triplets, which represents the global feature of the whole graph. The resulting graph representation can be formulated as

$$\mathbf{G}^\dagger = \{\mathcal{F}_O^B \circ \mathcal{F}_O^C \circ \mathcal{F}^{LLM}, \mathcal{F}_R \circ \mathcal{F}_R^C \circ \mathcal{F}^{LLM}\}, \quad (1)$$

where  $\circ$  indicates the concatenation operation. An example of this process has been demonstrated in Fig. 3.

### 3.2. Scene Graph Encoder

The encoder consists of a graph convolution network (GCN) and groups of MLP layers. GCN is exploited to pass information along graph edges of  $\mathbf{G}^\dagger$ . The extracted graph features are feed into a MLP layer, followed by additional two MLP heads which then separately output the means  $\mu$  and variances  $\sigma$  of the joint layout-shape distribution  $Z \sim \mathcal{N}(\mu, \sigma)$ . The training objective of the graph encoder is to minimize the Kullback-Liebler (KL) divergence between the posterior distribution  $p(z|x)$  and the model  $Z$ . The KL loss is formulated as:

$$\mathcal{L}_{KL} = D_{KL}(p(z|x) || E_G(z|x, \mathbf{G}^\dagger)). \quad (2)$$

Through re-parameterization, a random vector  $z$  can be sampled from  $Z$  for each graph node, and used to replace

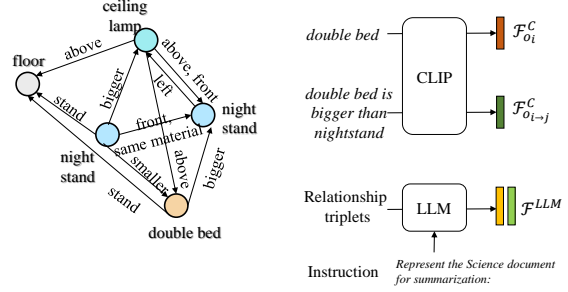


Figure 3. Example of scene graph representation construction process.

the layout features  $\mathcal{F}_B$  that only work for training phase. With the updated node features, the updated graph is as follows,

$$\mathbf{G}^\ddagger = \{\mathcal{F}_O \circ \mathcal{F}_O^z \circ \mathcal{F}_O^C \circ \mathcal{F}^{LLM}, \mathcal{F}_R \circ \mathcal{F}_R^C \circ \mathcal{F}^{LLM}\}. \quad (3)$$

To extract the updated graph features from  $\mathbf{G}^\ddagger$ , we employ a unified GCN so that the layout branch and the shape branch can interact with each other at an early stage.

### 3.3. 3D Scene Decoder

The decoder consists of a layout branch which produces scene layouts for spatial arrangements and a shape branch which samples 3D shapes for objects. The updated graph features are feed into three separate MLPs in parallel.

The BBox MLP is leveraged to predict the 6-parameterized 3D bounding box  $b_i$  including width, length, height and centroid coordinates. Similarly, the Angle MLP predicts the angular rotation  $\alpha_i$  along the vertical axis. The training objective of layout branch is,

$$\mathcal{L}_{layout} = \mathcal{L}_{rec} + \eta \mathcal{L}_{iou}. \quad (4)$$

where  $\mathcal{L}_{rec}$  and  $\mathcal{L}_{iou}$  denote the layout reconstruction loss and Intersection-over-Union (IoU) based regularization loss, respectively.  $\eta$  is used to balance these two loss items.

The reconstruction loss consists of 3D bounding box regression loss and rotation classification loss.

$$\mathcal{L}_{rec} = \frac{1}{N} \sum_{i=1}^N (|\hat{b}_i - b_i| - \sum_{j=1}^{\beta} \hat{\alpha}_i^j \log \alpha_i^j). \quad (5)$$

where  $\hat{b}_i$  and  $\hat{\alpha}_i$  are ground-truth 6-parameterized box and rotation. The rotation space is divided into  $\beta$  bins.

The regularization loss is introduced to avoid the layout collision by encouraging the similarity between predicted layout  $y_i = \{b_i \circ \alpha_i\}$  and the corresponding ground-truth layout  $\hat{y}_i = \{\hat{b}_i \circ \hat{\alpha}_i\}$ .

$$\mathcal{L}_{iou} = \sum_{i=1}^N (1 - IoU(\hat{y}_i, y_i)). \quad (6)$$

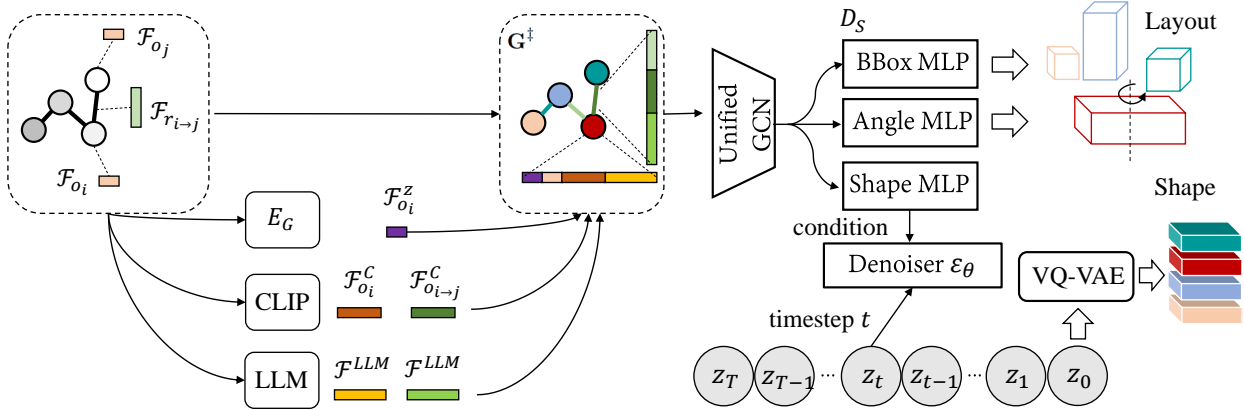


Figure 4. Overall pipeline for the inference phase. After integrating all the relationship triplets of the graph, LLM is utilized to generate a sentence embedding. With aggregated features for graph nodes and edges, the unified GCN achieves information passing along edges. The extracted graph features are feed into 3D scene decoder to simultaneously generate layouts and shapes for all graph nodes.

Regarding the shape branch, the Shape MLP outputs the shape codes  $c_s$  which act as the conditions for the following shape generation process. Truncated SDFs (TSDFs) [6] with resolution  $D_{SDF}$  are utilized to represent 3D shapes, which can be transformed to 3D meshes. Following baseline [38], a pretrained and frozen VQ-VAE [33] is utilized for encoding SDFs to shape latent  $z_0$  and decoding it back SDFs. The forward diffusion process gradually adds random noise to the shape latent  $z_0$ , and the reverse diffusion process denoises the noisy latent  $z_t$  back  $z_0$ . The time step  $t$  is sampled using  $T$  which is the maximum time steps. Conditioned on  $c_s$ , a 3D-UNet [5] is employed as the noise predictor (denoiser)  $\epsilon_\theta$  for the denoising process. The training objective is,

$$\mathcal{L}_{shape} = \|\epsilon - \epsilon_\theta(z_t, t, c_s)\|^2. \quad (7)$$

Overall, the training loss function is,

$$\mathcal{L} = \lambda_{KL} \mathcal{L}_{KL} + \lambda_{layout} \mathcal{L}_{layout} + \lambda_{shape} \mathcal{L}_{shape}. \quad (8)$$

where  $\lambda_{KL}$ ,  $\lambda_{layout}$  and  $\lambda_{shape}$  are weighting factors.

### 3.4. Inference

After training, our method can generate compositional 3D scenes from the given scene graphs. Note that ground-truth layouts are not required for inference. As illustrated in Fig. 4, the inference phase starts with constructing the updated scene graph representation  $\mathbf{G}^\ddagger$ .  $E_G$  is used to estimate the joint layout-shape distribution  $Z$ . By sampling random vectors  $z$  from  $Z$ , the feature vector  $\mathcal{F}_{o_i}^z$  is derived for the graph node  $o_i$ . At the same time, CLIP is employed to produce the feature vector  $\mathcal{F}_{o_i}^C$  for  $o_i$  and  $\mathcal{F}_{o_i \to j}^C$  for the edge  $r$  between node  $o_i$  and  $o_j$ . After integrating all the relationship triplets of the graph, LLM is utilized to generate a sentence embedding  $\mathcal{F}^{LLM}$ . With aggregated features

for graph nodes and edges, the unified GCN achieves information passing along edges. Then, the extracted graph features are feed into  $D_s$  to simultaneously generate layouts and shapes for all graph nodes  $O$ .

## 4. Experiments

In this section, we firstly clarify the experimental settings including dataset, evaluation metrics and implementation details. Then, the quantitative and qualitative results are shown and analyzed. Ablations studies are conducted to verify the effects of the proposed components.

### 4.1. Dataset and Evaluation Metrics

**Dataset.** Our method is validated on a recent benchmark dataset, named SG-FRONT [38], which extends the original 3D-FRONT dataset [10] with paired scene graph annotations. SG-FRONT dataset covers three room types of indoor scenes: 4,041 bedrooms, 900 dining rooms, and 813 living rooms. Following the original splits [38], 3,879 bedrooms, 614 dining rooms, and 544 living rooms are used for training, and the remaining ones are used for testing. Each room typically contains multiple objects, ending up with 45K object samples in total. The scene compositions are described by scene graphs, where nodes are defined by object semantics (categories) and edges are semantic relationships (predicates) between nodes. Overall, SG-FRONT dataset has 35 object categories and 15 relationship categories.

**Evaluation Metrics.** The synthesized 3D scenes are evaluated from three major aspects: **scene-level fidelity**, **scene graph consistency** and **object-level fidelity**. For the scene-level fidelity, we report Fréchet Inception Distance (FID)

Table 1. Comparisons with Graph-to-3D [7] and CommonScenes [38] on scene-level fidelity in SG-FRONT dataset [38] (lower is better). FID and KID ( $\times 0.001$ ) are computed based on the top-down images ( $256 \times 256$  pixels) rendered from the synthesized and reference 3D scenes. (\*) denotes the shape retrieval version of the method where only layout branch is utilized. The best results are shown in **bold**.

Method	Bedroom		Living room		Dining room		All	
	FID↓	KID↓	FID↓	KID↓	FID↓	KID↓	FID↓	KID↓
Graph-to-3D [7] (*)	<b>60.48</b>	<b>7.85</b>	81.31	3.97	67.40	5.88	<b>45.89</b>	<b>4.34</b>
CommonScenes [38] (*)	64.91	13.23	<b>78.24</b>	<b>2.65</b>	<b>65.48</b>	<b>4.13</b>	47.22	5.98
Graph-to-3D [7]	68.37	17.97	92.50	18.48	71.13	7.76	51.91	9.25
CommonScenes [38]	65.26	12.79	85.87	8.89	69.67	6.71	49.89	7.37
Ours	<b>60.47</b>	<b>9.30</b>	<b>82.99</b>	<b>8.51</b>	<b>69.40</b>	<b>6.39</b>	<b>47.34</b>	<b>6.13</b>

Table 2. Comparisons with Graph-to-3D [7] and CommonScenes [38] on scene graph consistency (higher is better). The best results are shown in **bold**.

Method	Easy				Hard		mSG
	<i>left/right</i> ↑	<i>front/behind</i> ↑	<i>big/small</i> ↑	<i>tall/short</i> ↑	<i>close</i> ↑	<i>symmetrical</i> ↑	
Graph-to-3D [7] (*)	<b>0.98</b>	0.99	0.96	0.93	0.74	0.50	0.87
CommonScenes [38] (*)	<b>0.98</b>	<b>1.00</b>	<b>0.97</b>	<b>0.96</b>	<b>0.76</b>	<b>0.62</b>	<b>0.90</b>
Graph-to-3D [7]	<b>0.98</b>	0.99	<b>0.97</b>	0.96	0.75	0.64	<b>0.90</b>
CommonScenes [38]	<b>0.98</b>	0.99	<b>0.97</b>	0.96	0.76	<b>0.66</b>	<b>0.90</b>
Ours	<b>0.98</b>	<b>1.00</b>	<b>0.97</b>	<b>0.97</b>	<b>0.77</b>	<b>0.66</b>	<b>0.90</b>

[12] and Kernel Inception Distance (KID) [1] between top-down renderings of the synthesized and reference 3D scenes. Based on geometric constraints [7], the scene graph consistency is measured to assess the spatial consistency between the generated layouts and the corresponding relationships specified in the given graph edges. Following CommonScenes [38], we validate easy edges with basic relationships (including *left/right*, *front/behind*, *bigger/smaller than*, *taller/shorter than*), as well as hard edges with proximity relationships (including *close by* and *symmetrical to*). In addition, object-level shape fidelity is reported by Chamfer Distance (CD) [9] based Minimum Matching Distance (MMD), Coverage (COV), and 1-Nearest Neighbor Accuracy (1-NNA) [37], which are computed using 3D point clouds sampled from the generated shapes and the reference shapes.

## 4.2. Implementation Details

All the experiments are conducted on a single NVIDIA A40 GPU with 46GB memory. We set the feature embedding dimension  $Q = 64$ . For scene graph encoder  $E_G$ , 5 GCN layers are exploited to extract graph  $\mathbf{G}^\dagger$  features which are then feed with two groups of MLP layers. Each group consists of a MLP followed by two separate MLP heads to predict  $\mu$  and  $\sigma$ , respectively. These two groups output 48-dimensional and 16-dimensional feature vectors in parallel. After the concatenation process, the resulting  $\mu$  and  $\sigma$  are 64-dimensional and the distribution  $Z$  is 64-dimensional Gaussian distribution.  $\mathcal{F}_B$  is only used for training and not needed for inference phase, and the inference starts from the updated scene graph representation  $\mathbf{G}^\dagger$ . A unified GCN which consists of 5 layers without sharing

parameters with the GCNs of  $E_G$ , is employed at the bottleneck part between scene graph encoder  $E_G$  and 3D scene decoder  $D_S$ . BBox MLP module, Angle MLP module and Shape MLP module take the extracted graph features as inputs. There are 3 stacked MLP layers for each MLP module. The weighting factors  $\lambda_{KL}$ ,  $\lambda_{layout}$ ,  $\lambda_{shape}$  are set to 1.0, while  $\eta$  is set to 0.01. For the rotation classification,  $\beta$  is set to 24. Shape code  $c_s$  is a 1280-dimensional vector, which conditions the denoiser  $\epsilon_\theta$ . The resolution of SDF is 64, i.e.  $SDF \in \mathbb{R}^{64 \times 64 \times 64}$ . The shape latent  $z_0 \in \mathbb{R}^{16 \times 16 \times 16}$ . For the latent diffusion model, time step  $T$  is set to 100. The whole framework is trained in an end-to-end manner with the AdamW optimizer [21] and the initial learning rate is set to  $1e^{-4}$ .

## 4.3. Quantitative Results and Comparison

The proposed method is compared with two recent state-of-the-art scene graph-to-3D scene synthesis methods: Graph-to-3D [7] and CommonScenes [38]<sup>1</sup>.

First, we report the results on scene-level fidelity, as shown in Table 1. The top two rows are shape retrieval-based methods (i.e., only layout branch is trained and tested) and the bottom three are joint shape and layout learning-based methods. Since 3D shapes are directly retrieved from the database, the retrieval-based methods (\*) usually achieve lower FIDs and KIDs than (semi-) generative methods. However, shape retrieval-based methods are heavily bounded by the scale and reliability of the given databases. For all the room types, our method has 47.34

<sup>1</sup>All the results of Graph-to-3D [7] and CommonScenes [38] presented in this paper are reproduced using the official code with default settings.

Table 3. Comparisons with Graph-to-3D [7] and CommonScenes [38] on object-level fidelity. MMD ( $\times 0.01$ ), COV (%) and 1-NNA (%) are computed. Total is calculated as the mean values across categories. The best results are shown in **bold**.

Category	MMD $\downarrow$			COV $\uparrow$			1-NNA $\downarrow$		
	[7]	[38]	Ours	[7]	[38]	Ours	[7]	[38]	Ours
Bed	<b>1.27</b>	1.47	1.73	<b>10.34</b>	5.17	4.31	97.41	<b>92.62</b>	93.44
Nightstand	<b>3.00</b>	7.12	4.49	<b>11.21</b>	6.03	6.03	98.28	<b>93.60</b>	<b>93.60</b>
Wardrobe	<b>1.15</b>	3.11	1.41	<b>7.76</b>	2.59	6.03	97.41	97.56	<b>91.87</b>
Chair	<b>2.28</b>	2.57	3.10	8.62	<b>9.48</b>	6.90	97.41	<b>93.23</b>	<b>93.23</b>
Table	5.68	4.98	<b>4.27</b>	8.62	<b>12.07</b>	10.34	96.98	<b>86.57</b>	88.06
Cabinet	2.57	3.45	<b>2.41</b>	5.17	5.17	<b>9.48</b>	96.45	96.21	<b>88.64</b>
Lamp	4.00	2.78	<b>2.44</b>	7.76	10.34	<b>12.07</b>	98.71	86.86	<b>81.75</b>
Shelf	6.60	5.43	<b>3.14</b>	6.67	20.00	<b>26.67</b>	96.00	<b>56.52</b>	65.22
Sofa	1.31	1.11	<b>1.08</b>	0.86	6.90	<b>9.48</b>	99.04	<b>93.75</b>	96.88
TV stand	0.98	<b>0.62</b>	0.84	2.59	<b>12.93</b>	6.03	98.02	<b>90.91</b>	94.70
Total	2.88	3.26	<b>2.49</b>	6.96	9.07	<b>9.73</b>	97.57	88.78	<b>88.74</b>

Table 4. Ablation studies. Unified GCN and sparate GCN are abbreviated as Uni and Sep, respectively. The best results are shown in **bold**, and the second best results are shown with underlines.

$D_{box}$	Settings			Scene fidelity		Scene graph consistency		
	GCN	LLM	IoU	FID $\downarrow$	KID $\downarrow$	<i>close</i> $\uparrow$	<i>symmetrical</i> $\uparrow$	mSG $\uparrow$
×	Sep	×	×	48.20	6.73	0.72	0.56	0.88
✓	Sep	×	×	49.89	7.37	0.76	<b>0.66</b>	<u>0.90</u>
×	Uni	×	×	51.63	11.06	0.76	0.59	0.89
✓	Uni	×	×	<u>47.69</u>	<u>6.54</u>	<u>0.78</u>	0.59	0.89
×	Uni	✓	×	48.15	6.93	0.76	<u>0.62</u>	<u>0.90</u>
✓	Uni	✓	×	49.09	8.74	<b>0.79</b>	<b>0.66</b>	<b>0.91</b>
×	Uni	✓	✓	<b>47.34</b>	<b>6.13</b>	0.77	<b>0.66</b>	<u>0.90</u>

FID score and 6.13 KID score. Compared to the Graph-to-3D approach [7], our method has reached 4.57 lower FID score, 3.12 lower KID score. Compared to the state-of-the-art CommonScenes [38], our method has reached 2.55 lower FID score, 1.24 lower KID score. Overall, our method obtains the best FID and KID scores on all the room types (lower score indicates better performance). Surprisingly, our method even achieves the best performance with retrieval-based methods on the FID score in Bedroom scenes.

Second, we report the performance in terms of scene graph consistency, as shown in Table 2. The proposed method achieves the best results on all the metrics. In general, with joint layout-shape learning frameworks, (semi-) generative methods derive better consistency than retrieval-based methods (\*) that only learn layout generation.

Finally, we provide object-level fidelity comparisons of shape generative methods. Table 3 shows the results of 10 object categories on MMD, COV and 1-NNA. In terms of MMD score (lower is better), our method is 0.39 lower than Graph-to-3D [7] and 0.77 lower than CommonScenes [38]. In terms of COV score (higher is better), our method is 2.77 higher than Graph-to-3D [7] and 0.7 higher than CommonScenes [38]. In terms of 1-NNA score (lower is better), our method is 8.83 lower than Graph-to-3D [7] and 0.04

lower than CommonScenes [38]. Overall, our method attains better results compared to Graph-to-3D [7] and CommonScenes [38], which suggests the object-level shape generation ability of the proposed method.

#### 4.4. Ablation Study

We perform ablation studies to verify the effects of different components in the proposed framework. Using the metrics in terms of scene-level fidelity and scene graph consistency, we quantitatively evaluate different configurations in Table 4, where the presence and absence of the components are marked via check marks and cross marks, respectively. Note that the mean scene graph consistency mSG values are computed on both easy and hard relationships. The results of simple relationships are provided in the supplementary material.

**Discriminator.** Discriminator  $D_{box}$  is commonly used in previous works [7, 38] to model the one-to-many problem of self-supervised learning layout generation. By comparing the results with and without  $D_{box}$  (keep other settings consistent), we observe that  $D_{box}$  brings benefits for the scene graph consistency, which shows its necessity for layout reconstruction. However, GAN-based architectures may suffer from training instability. For example,  $D_{box}$  fails

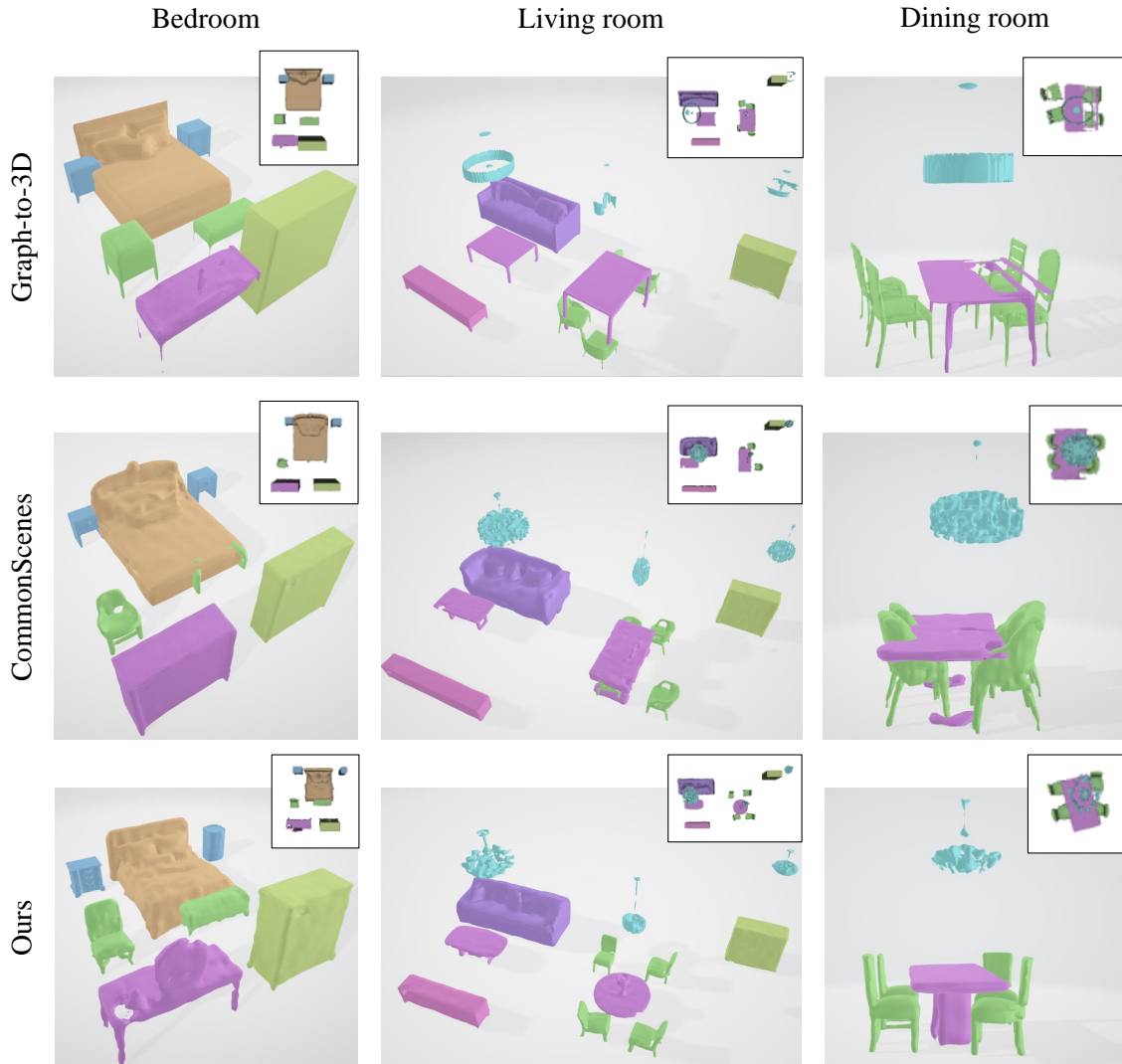


Figure 5. Qualitative examples of bedroom, living room and dining room. Compared to Graph-to-3D [7] and CommonScenes [38], our method shows higher fidelity with less interpenetrating phenomena.

to improve the scene-level fidelity, as shown in the first two rows of Table 4.

**Unified GCN vs. Separate GCN.** With the assistance of  $D_{box}$ , the unified GCN outperforms the separate GCNs on the scene-level fidelity (4th row vs. 2nd row). Besides, it can be seen from the 3rd row that, only using an individual GCN (i.e., unified GCN) without other designs (e.g., LLM-enhanced scene graph representation) may lead to insufficient guidance for scene decoder.

**LLM-enhanced scene graph representation.** This representation provides strong signal at the encoding stage. As shown in the 3rd and 5th rows, LLM-based graph encoding introduces significant improvements. With  $D_{box}$  (the 6th row), the scene graph consistency can be further

improved while scene-level fidelity decreases, which also demonstrates the instability of  $D_{box}$ .

**IoU-based layout regularization.** Compared the 5th row to the 8th, the layout regularization performs better on all metrics. Through the comparisons between last two rows, the proposed regularization is more robust than the discriminator and obtains great improvements in scene-level fidelity.

#### 4.5. Qualitative Results and Comparison

Qualitative results are shown in Fig. 5 and Fig. 6. More results are provided in the supplementary material.

Graph-to-3D [7] and CommonScenes [38] tend to synthesize unrealistic 3D scenes in which ambiguous shapes (e.g., broken dining table) and interpenetrating phenom-



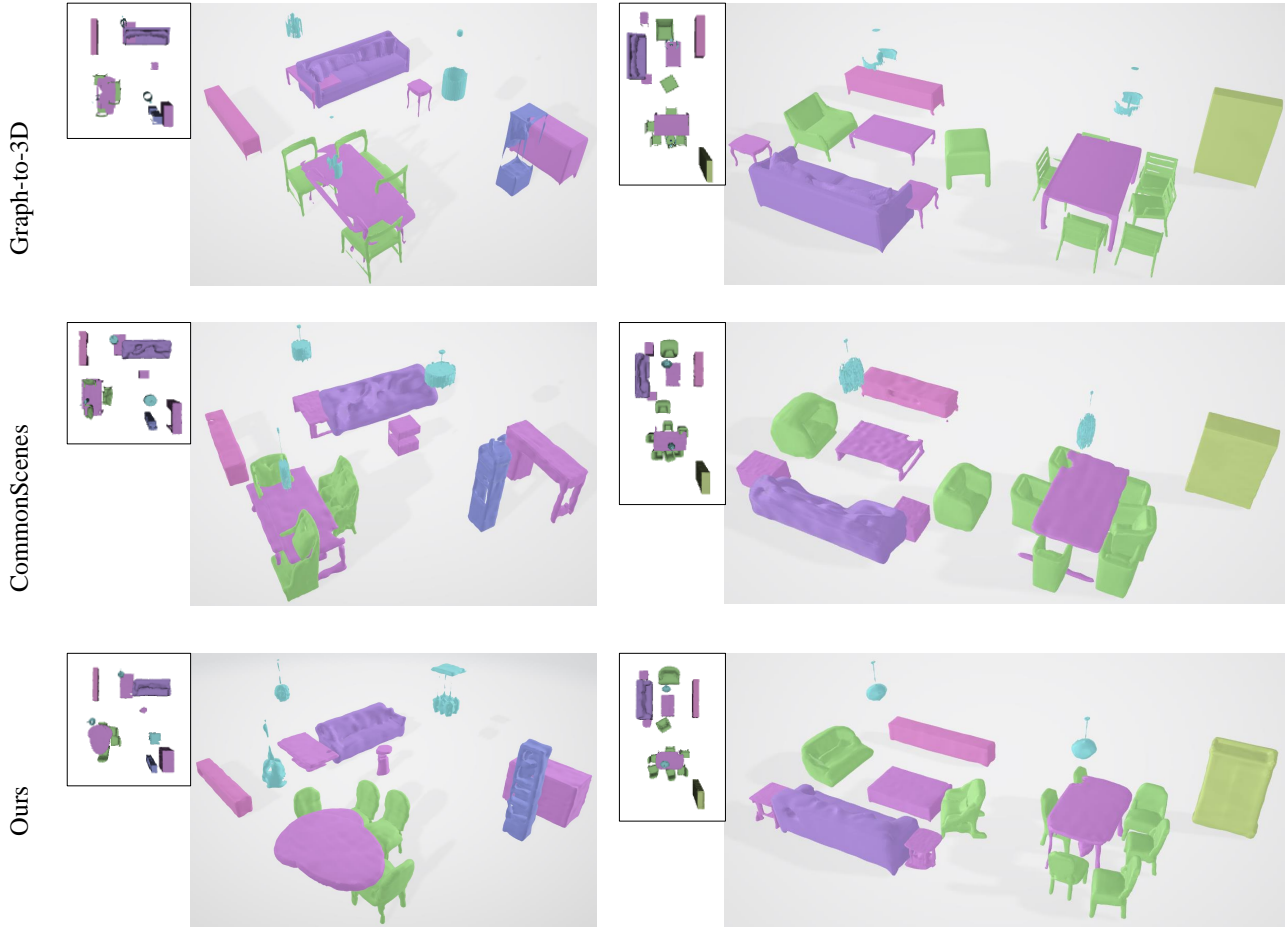


Figure 6. Additional qualitative examples of living room and dining room.

ena (e.g., table and chair intersect with each other) commonly happen. In contrast, our method is able to generate much more realistic 3D scenes with reasonable spatial arrangements and shape generation. On one hand, our layout generation is constrained with IoU-based regularization, which efficiently alleviates object collision problems compared to those un-regularized layout regression approaches, as shown in Fig. 6. On the other hand, we notice that the 3D shapes generated from our method are not as random as prior works. It can be seen from the table-and-chair cases in Fig. 5, the table is generated as round shape (in living room) or with single table leg (in dining room), which match the arrangements of the surrounding chairs. Without special designs, our shape branch benefits from the proposed LLM-enhanced scene graph representation, the unified GCN for joint layout-shape learning, as well as the regularized spatial arrangements.

## 5. Conclusions

In this work, we present a novel scene graph-to-3D scene synthesis method which alleviates layout collision problems existed in prior works. With LLM better understanding of object-object and scene-object relationships, more reasonable 3D scene synthesis is achieved at both object level and scene level. A regularization loss is introduced to guide the layout regression. Layout branch and shape branch, which share the graph features from a unified GCN, are jointly optimized in an end-to-end manner. Compared to the state-of-the-art CommonScenes approach, our method has reached 2.55 lower Fréchet Inception Distance (FID) score and 1.24 lower Kernel Inception Distance (KID) score on the SGFRONT dataset. For future work, we will work on collision-free compositional scene synthesis and explore other user-friendly condition inputs, such as free-form descriptions or few specified relationships.

## References

- [1] Miłkołaj Bińkowski, Danica J Sutherland, Michael Arbel, and Arthur Gretton. Demystifying mmd gans. *ICLR*, 2018. 6
- [2] Mu Cai, Yixiao Ge, Zhuohan Li, Zijian Wang, Yikang Shen, Demi Guo, Yiming Cui, Bin Zhao, Hao Zhang, Jianfeng Wang, and Yizhou Wang. Making large multimodal models understand arbitrary visual prompts. *arXiv 2312.00784*, 2023. 3
- [3] Angel X Chang, Thomas Funkhouser, Leonidas Guibas, Pat Hanrahan, Qixing Huang, Zimo Li, Silvio Savarese, Manolis Savva, Shuran Song, Hao Su, et al. Shapenet: An information-rich 3d model repository. *arXiv preprint arXiv:1512.03012*, 2015. 3
- [4] Yen-Chi Cheng, Hsin-Ying Lee, Sergey Tulyakov, Alexander G Schwing, and Liang-Yan Gui. Sdfusion: Multimodal 3d shape completion, reconstruction, and generation. In *Proceedings of the IEEE/CVF Conference on Computer Vision and Pattern Recognition*, pages 4456–4465, 2023. 1
- [5] Özgün Çiçek, Ahmed Abdulkadir, Soeren S Lienkamp, Thomas Brox, and Olaf Ronneberger. 3d u-net: learning dense volumetric segmentation from sparse annotation. In *Medical Image Computing and Computer-Assisted Intervention—MICCAI 2016: 19th International Conference, Athens, Greece, October 17-21, 2016, Proceedings, Part II 19*, pages 424–432. Springer, 2016. 5
- [6] Brian Curless and Marc Levoy. A volumetric method for building complex models from range images. In *Proceedings of the 23rd annual conference on Computer graphics and interactive techniques*, pages 303–312, 1996. 5
- [7] Helisa Dhama, Fabian Manhardt, Nassir Navab, and Federico Tombari. Graph-to-3d: End-to-end generation and manipulation of 3d scenes using scene graphs. In *Proceedings of the IEEE/CVF International Conference on Computer Vision*, pages 16352–16361, 2021. 1, 2, 3, 6, 7, 8, 12, 13
- [8] Francis Engelmann, Konstantinos Rematas, Bastian Leibe, and Vittorio Ferrari. From points to multi-object 3d reconstruction. In *Proceedings of the IEEE/CVF conference on computer vision and pattern recognition*, pages 4588–4597, 2021. 1, 2
- [9] Haoqiang Fan, Hao Su, and Leonidas J Guibas. A point set generation network for 3d object reconstruction from a single image. In *Proceedings of the IEEE conference on computer vision and pattern recognition*, pages 605–613, 2017. 6
- [10] Huan Fu, Bowen Cai, Lin Gao, Ling-Xiao Zhang, Jiaming Wang, Cao Li, Qixun Zeng, Chengyue Sun, Rongfei Jia, Bin-qiang Zhao, et al. 3d-front: 3d furnished rooms with layouts and semantics. In *Proceedings of the IEEE/CVF International Conference on Computer Vision*, pages 10933–10942, 2021. 5
- [11] Ian Goodfellow, Jean Pouget-Abadie, Mehdi Mirza, Bing Xu, David Warde-Farley, Sherjil Ozair, Aaron Courville, and Yoshua Bengio. Generative adversarial nets. *Advances in neural information processing systems*, 27, 2014. 1
- [12] Martin Heusel, Hubert Ramsauer, Thomas Unterthiner, Bernhard Nessler, and Sepp Hochreiter. Gans trained by a two time-scale update rule converge to a local nash equilibrium. *NeurIPS*, 30, 2017. 6
- [13] Jonathan Ho, Ajay Jain, and Pieter Abbeel. Denoising diffusion probabilistic models. *Advances in neural information processing systems*, 33:6840–6851, 2020. 1
- [14] Heewoo Jun and Alex Nichol. Shap-e: Generating conditional 3d implicit functions. *arXiv preprint arXiv:2305.02463*, 2023. 1
- [15] Diederik P Kingma and Max Welling. Auto-encoding variational bayes. *arXiv preprint arXiv:1312.6114*, 2013. 1
- [16] Anna Kukleva, Hilde Kuehne, Fadime Sener, and Juergen Gall. Howtocation: Prompting llms to transform video annotations at scale. *arXiv preprint arXiv:2310.04900*, 2023. 3
- [17] Haotian Liu, Chunyuan Li, Qingyang Wu, Yong Jae Lee, Jianwei Yang, Yong Zhang, Houdong Hu, Zicheng Liu, and Jianfeng Gao. Visual instruction tuning. *arXiv 2304.08485*, 2023. 3
- [18] Minghua Liu, Chao Xu, Haian Jin, Linghao Chen, Mukund Varma T, Zexiang Xu, and Hao Su. One-2-3-45: Any single image to 3d mesh in 45 seconds without per-shape optimization. *Advances in Neural Information Processing Systems*, 36, 2024. 1
- [19] Ruoshi Liu, Rundi Wu, Basile Van Hoorick, Pavel Tokmakov, Sergey Zakharov, and Carl Vondrick. Zero-1-to-3: Zero-shot one image to 3d object. In *Proceedings of the IEEE/CVF International Conference on Computer Vision*, pages 9298–9309, 2023. 1
- [20] Zhengzhe Liu, Peng Dai, Ruihui Li, Xiaojuan Qi, and Chi-Wing Fu. Iss: Image as setting stone for text-guided 3d shape generation. *arXiv preprint arXiv:2209.04145*, 2022. 1
- [21] Ilya Loshchilov and Frank Hutter. Decoupled weight decay regularization. In *International Conference on Learning Representations*, 2019. 6
- [22] Andrew Luo, Zhoutong Zhang, Jiajun Wu, and Joshua B Tenenbaum. End-to-end optimization of scene layout. In *Proceedings of the IEEE/CVF Conference on Computer Vision and Pattern Recognition*, pages 3754–3763, 2020. 1, 2
- [23] Ben Mildenhall, Pratul P. Srinivasan, Matthew Tancik, Jonathan T. Barron, Ravi Ramamoorthi, and Ren Ng. Nerf: Representing scenes as neural radiance fields for view synthesis. In *ECCV*, 2020. 3
- [24] Subhabrata Mukherjee, Arindam Mitra, Ganesh Jawahar, Sahaj Agarwal, Hamid Palangi, and Ahmed Awadallah. Orca: Progressive learning from complex explanation traces of gpt-4. *arXiv 2306.02707*, 2023. 3
- [25] Ryan Po and Gordon Wetzstein. Compositional 3d scene generation using locally conditioned diffusion. *arXiv preprint arXiv:2303.12218*, 2023. 1, 2, 3
- [26] Alec Radford, Jong Wook Kim, Chris Hallacy, Aditya Ramesh, Gabriel Goh, Sandhini Agarwal, Girish Sastry, Amanda Askell, Pamela Mishkin, Jack Clark, et al. Learning transferable visual models from natural language supervision. In *International conference on machine learning*, pages 8748–8763. PMLR, 2021. 4
- [27] Aditya Ramesh, Prafulla Dhariwal, Alex Nichol, Casey Chu, and Mark Chen. Hierarchical text-conditional image generation with clip latents. *arXiv preprint arXiv:2204.06125*, 1(2):3, 2022. 1

- [28] Xuanchi Ren, Jiahui Huang, Xiaohui Zeng, Ken Museth, Sanja Fidler, and Francis Williams. Xcube: Large-scale 3d generative modeling using sparse voxel hierarchies. *arXiv preprint arXiv:2312.03806*, 2023. [1](#), [2](#), [3](#)
- [29] Danilo Rezende and Shakir Mohamed. Variational inference with normalizing flows. In *International conference on machine learning*, pages 1530–1538. PMLR, 2015. [1](#)
- [30] Hongjin Su, Weijia Shi, Jungo Kasai, Yizhong Wang, Yushi Hu, Mari Ostendorf, Wen-tau Yih, Noah A Smith, Luke Zettlemoyer, and Tao Yu. One embedder, any task: Instruction-finetuned text embeddings. *arXiv preprint arXiv:2212.09741*, 2022. [4](#)
- [31] Jiaxiang Tang, Jiawei Ren, Hang Zhou, Ziwei Liu, and Gang Zeng. Dreamgaussian: Generative gaussian splatting for efficient 3d content creation. *arXiv preprint arXiv:2309.16653*, 2023. [1](#)
- [32] Xi Tian, Yong-Liang Yang, and Qi Wu. Shapescollider: Structure-aware 3d shape generation from text. In *Proceedings of the IEEE/CVF International Conference on Computer Vision*, pages 2715–2724, 2023. [1](#)
- [33] Aaron Van Den Oord, Oriol Vinyals, et al. Neural discrete representation learning. *Advances in neural information processing systems*, 30, 2017. [5](#)
- [34] Xueyang Wang, Xiangteng Zeng, Ali Ghadirzadeh, Yue Yin, Trevor Darrell, and Chelsea Finn. Maxi: Multi-axis instructional videos. In *Proceedings of the IEEE/CVF Conference on Computer Vision and Pattern Recognition*, pages 22704–22714, 2022. [3](#)
- [35] Yao Wei, George Vosselman, and Michael Ying Yang. Flow-based gan for 3d point cloud generation from a single image. *BMVC*, 2022. [1](#)
- [36] Xinyu Yan, Yuxiao Hu, Peiyu Zhao, Xiaojun Zhu, Yaguang Guo, Zihao Wang, Changqing Xu, Dacheng Tao, Zheng Shen, Xinwei Geng, et al. Internvideo: General video foundation models via generative and discriminative learning. *arXiv preprint arXiv:2212.03191*, 2022. [3](#)
- [37] Guandao Yang, Xun Huang, Zekun Hao, Ming-Yu Liu, Serge Belongie, and Bharath Hariharan. Pointflow: 3d point cloud generation with continuous normalizing flows. In *Proceedings of the IEEE/CVF international conference on computer vision*, pages 4541–4550, 2019. [6](#)
- [38] Guangyao Zhai, Evin Pinar Örnek, Shun-Cheng Wu, Yan Di, Federico Tombari, Nassir Navab, and Benjamin Busam. Commonsences: Generating commonsense 3d indoor scenes with scene graphs. *Advances in Neural Information Processing Systems*, 36, 2023. [1](#), [2](#), [3](#), [4](#), [5](#), [6](#), [7](#), [8](#), [12](#), [13](#)
- [39] Linqi Zhou, Yilun Du, and Jiajun Wu. 3d shape generation and completion through point-voxel diffusion. In *Proceedings of the IEEE/CVF International Conference on Computer Vision*, pages 5826–5835, 2021. [1](#)
- [40] Deyao Zhu, Jun Chen, Xiaoqian Shen, Xiang Li, and Mohamed Elhoseiny. Minigt-4: Enhancing vision-language understanding with advanced large language models. *arXiv 2304.10592*, 2023. [3](#)

## 6. Appendix

We present i) additional quantitative results in Appendix. 6.1, ii) user studies in Appendix. 6.2, and iii) additional qualitative results in Appendix. 6.3.

### 6.1. Additional Quantitative Results

Table 5 provides additional results on the easy scene graph consistency with simple relationships. All the settings perform well on *left/right* and *big/small*. As can be seen from the first four rows, the proposed unified GCN introduces slight improvements on *front/behind*. Besides, the proposed LLM-based scene graph representation contributes 0.03 (0.01) *tall/short* improvements without (with) the discriminator  $D_{box}$ . Thanks to the proposed IoU-based regularization, Ours (i.e., the last row) obtains the best performance without relying on  $D_{box}$  which is commonly used by previous works [7, 38] and has shown training instability.

Next, we introduce the implementation details of the evaluation metrics, including scene graph consistency and object-level fidelity.

The computation of scene graph consistency is defined by geometric rules depicted in Table 6, where  $IoU(\cdot)$ ,  $Cor(\cdot)$ ,  $Dis(\cdot)$  and  $Fli(\cdot)$  denote the processes of calculating Intersection-over-Unions, bounding box corners, distances, and flipping based on  $x$ -axis or  $y$ -axis, respectively. Besides,  $c$ ,  $w$ ,  $l$  and  $h$  indicate the bottom center coordinates, width, length and height of layout, i.e., bounding box  $b$ .

Given the set of point clouds  $S_g$  sampled from the generated 3D shapes and the set of reference point clouds  $S_r$  sampled from the reference shapes, MMD, COV and 1-NNA can be computed based on the Chamfer Distance (CD).

$$CD(X, Y) = \sum_{x \in X} \min_{y \in Y} \|x - y\|_2^2 + \sum_{y \in Y} \min_{x \in X} \|x - y\|_2^2. \quad (9)$$

where  $X$  and  $Y$  are two point clouds with the same number of points, and  $x$  and  $y$  indicate two points from different point clouds.

$$MMD(S_g, S_r) = \frac{1}{|S_r|} \sum_{Y \in S_r} \min_{X \in S_g} CD(X, Y). \quad (10)$$

$$COV(S_g, S_r) = \frac{|\{argmin_{Y \in S_r} CD(X, Y) | X \in S_g\}|}{|S_r|}. \quad (11)$$

$$1 - NNA(S_g, S_r) = \frac{\sum_{X \in S_g} \mathbb{I}[N_X \in S_g] + \sum_{Y \in S_r} \mathbb{I}[N_Y \in S_r]}{|S_g| + |S_r|}. \quad (12)$$

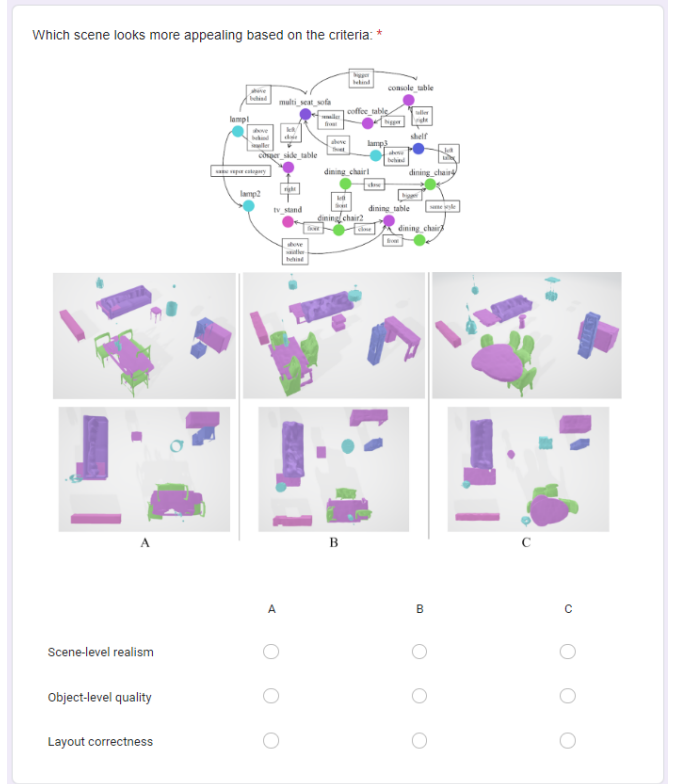


Figure 7. User interface for the user study.

where  $\mathbb{I}[\cdot]$  is the indicator function, and  $N_X$  is the CD-based nearest neighbor of  $X$  in  $S_{-X} = S_r \cup S_g - \{X\}$ .

### 6.2. User Study

Although the evaluation metrics can indicate the quality of the generated 3D scenes, they cannot be fully equated with human perception. Therefore, we invited  $\sim 30$  participants from various professional backgrounds to perform a user study as [38] did. Fig. 7 shows the user interface of this study.

Overall, we randomly sampled 15 scenes covering all room types, and the synthesized 3D scenes were the results of Graph-to-3D [7], CommonScenes [38] and the proposed method, respectively. To ensure the visibility, the scenes were rendered from a side view and a top-down view. Due to space limitation, only parts of relationships (i.e., edges) are shown in the scene graphs. Given the paired scene graph input and the 3D scenes synthesized by different methods, participants were requested to vote for the best scene based on three criteria: scene-level realism (SR), object-level quality (OQ), and layout correctness (LC). They were described to the participants by:

**SR:** Does the scene look realistic and stylistically coherent?

**OQ:** Do the objects have high-quality 3D shapes?

**LC:** Does the spatial arrangement of objects appear correct and free of collision?

Table 5. Ablation studies on the easy relationships. Unified GCN and sparate GCN are abbreviated as Uni and Sep, respectively. The best results are shown in **bold**.

$D_{box}$	Settings			Easy			
	GCN	LLM	IoU	<i>left/right</i> ↑	<i>front/behind</i> ↑	<i>big/small</i> ↑	<i>tall/short</i> ↑
×	Sep	×	×	<b>0.98</b>	0.99	<b>0.97</b>	0.94
✓	Sep	×	×	<b>0.98</b>	0.99	<b>0.97</b>	0.96
×	Uni	×	×	<b>0.98</b>	0.99	<b>0.97</b>	0.94
✓	Uni	×	×	<b>0.98</b>	<b>1.00</b>	<b>0.97</b>	0.96
×	Uni	✓	×	<b>0.98</b>	0.99	<b>0.97</b>	<b>0.97</b>
✓	Uni	✓	×	<b>0.98</b>	<b>1.00</b>	<b>0.97</b>	<b>0.97</b>
×	Uni	✓	✓	<b>0.98</b>	<b>1.00</b>	<b>0.97</b>	<b>0.97</b>

Table 6. Definitions of geometric constraints between two instances  $i$  and  $j$ .

Relationship	Rule
<i>left of</i>	$c_{x,i} < c_{x,j}$ and $IoU(b_i, b_j) < 0.3$
<i>right of</i>	$c_{x,i} > c_{x,j}$ and $IoU(b_i, b_j) < 0.3$
<i>front of</i>	$c_{y,i} < c_{y,j}$ and $IoU(b_i, b_j) < 0.3$
<i>behind of</i>	$c_{y,i} > c_{y,j}$ and $IoU(b_i, b_j) < 0.3$
<i>bigger than</i>	$(w_i l_i h_i - w_j l_j h_j) / w_i l_i h_i > 0.15$
<i>smaller than</i>	$(w_i l_i h_i - w_j l_j h_j) / w_i l_i h_i < -0.15$
<i>taller than</i>	$((c_{z,i} + h_i) - (c_{z,j} + h_j)) / (c_{z,i} + h_i) > 0.1$
<i>shorter than</i>	$((c_{z,i} + h_i) - (c_{z,j} + h_j)) / (c_{z,i} + h_i) < -0.1$
<i>close by</i>	$Dis(Cor(b_i), Cor(b_j)) < 0.45$
<i>symmetrical to</i>	$Dis(FLi(b_i), b_j) < 0.45$

Basically, SR requires participants to check whether the scene is realistic and coherent, acting as a global indicator that considers both 3D shapes and layouts. OQ emphasizes the completeness and fidelity of the generated object shapes, while LC denotes the spatial arrangement levels of objects.

The average results are given in Table 7. Most of the participants (48.3%) suggested that our generated scenes were preferred over the other methods on the scene-level realism. Where Graph-to-3D was instead preferred 42.5% and CommonScenes was preferred 9.2%. Regarding the object-level quality, most of the participants (49.7%) preferred the results of Graph-to-3D, without being informed that the inflexibility of its shape generation which relies on pre-trained shape codes from category-wise auto-decoders. CommonScenes and our method were preferred 10% and 40.3%, respectively. Furthermore, our method was preferred 60.5% on the layout correctness, much higher than other methods Graph-to-3D 31.7% and CommonScenes 7.8%, demonstrating its superiority on spatial arrangements of objects. Interestingly, our baseline method CommonScenes obtained the lowest voting rates on all the criteria of this study, even it outperformed Graph-to-3D on the evaluation metrics shown in the main paper. This perceptual user study shows that the proposed method improves compositional 3D scene synthesis compared to the baselines, and enjoys high flexibility without being dependent on perceptual shape codes and adversarial training.

Table 7. User study results via the percentage of voters.

Method	SR	OQ	LC
Graph-to-3D [7]	42.5%	49.7%	31.7%
CommonScenes [38]	9.2%	10.0%	7.8%
Ours	48.3%	40.3%	60.5%

### 6.3. Additional Qualitative Results

In Figs. 8, 9 and 10, we show additional qualitative results on the bedroom, living room and dining room scenes, respectively. Graph-to-3D [7] usually generates 3D scenes composed of regular object shapes and performs well for simple scenes such as bedrooms. However, the quality of generated objects degrades as the number of objects increases, e.g., on living rooms and dining rooms. Besides, it is observed that Graph-to-3D suffers from limited shape diversity. For instance, Graph-to-3D generates a specific 3D shape for the object *lamp* across different scenes. In contrast, the lamps generated from CommonScenes [38] have higher shape diversity. Benefiting from the diffusion-based shape branch, CommonScenes is able to synthesize diverse and plausible 3D shapes, but the generated scenes are often unrealistic due to low-quality shapes and object collisions. Compared to Graph-to-3D and CommonScenes, our method performs better at object level and scene level. It is worth pointing out that the 3D scenes generated by the proposed method exhibit more realistic shapes and reasonable layout configurations.



Figure 8. Additional qualitative comparisons on bedroom scenes. A side view of each 3D scene is provided with a top-down view.

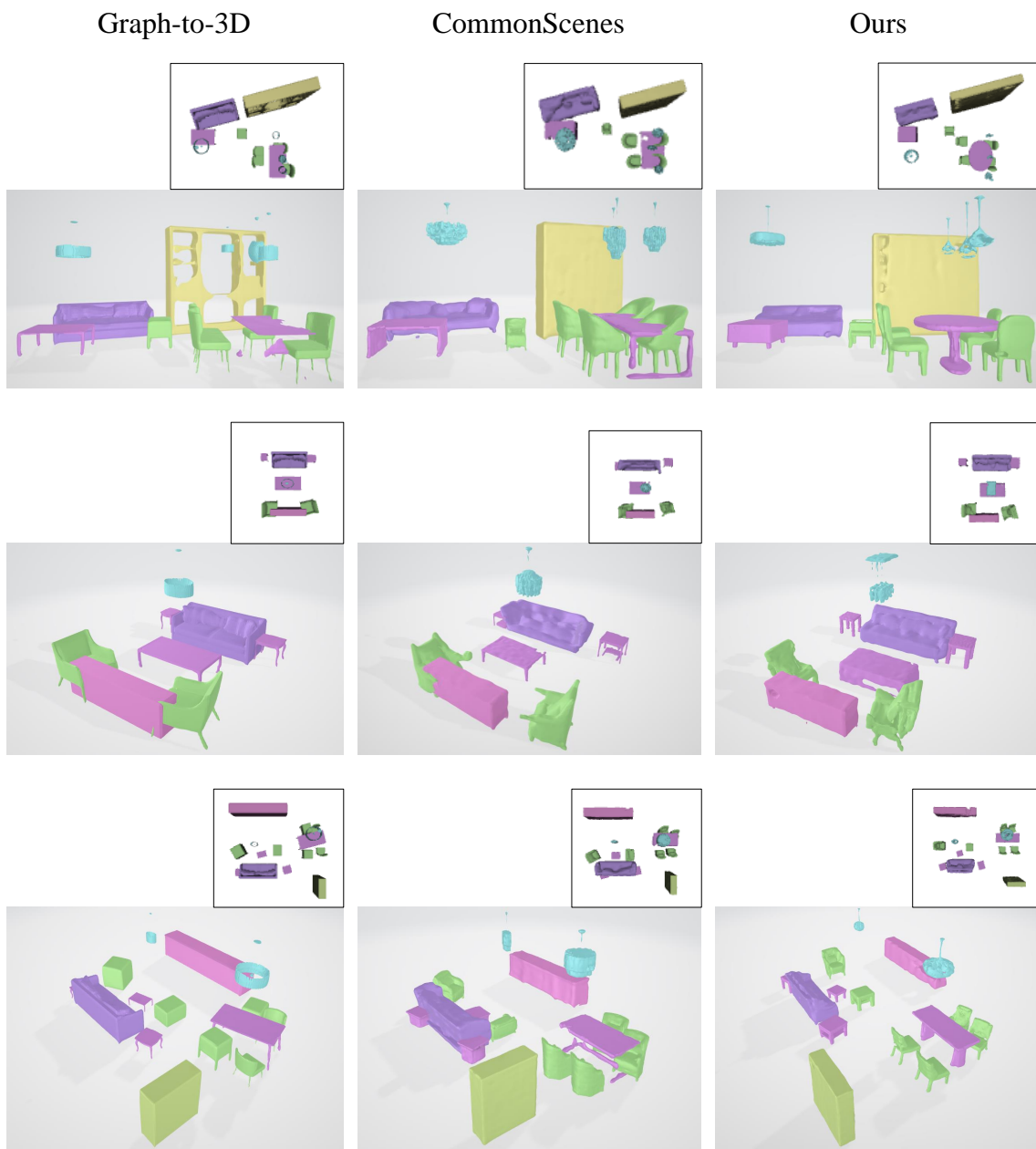


Figure 9. Additional qualitative comparisons on living room scenes. A side view of each 3D scene is provided with a top-down view.

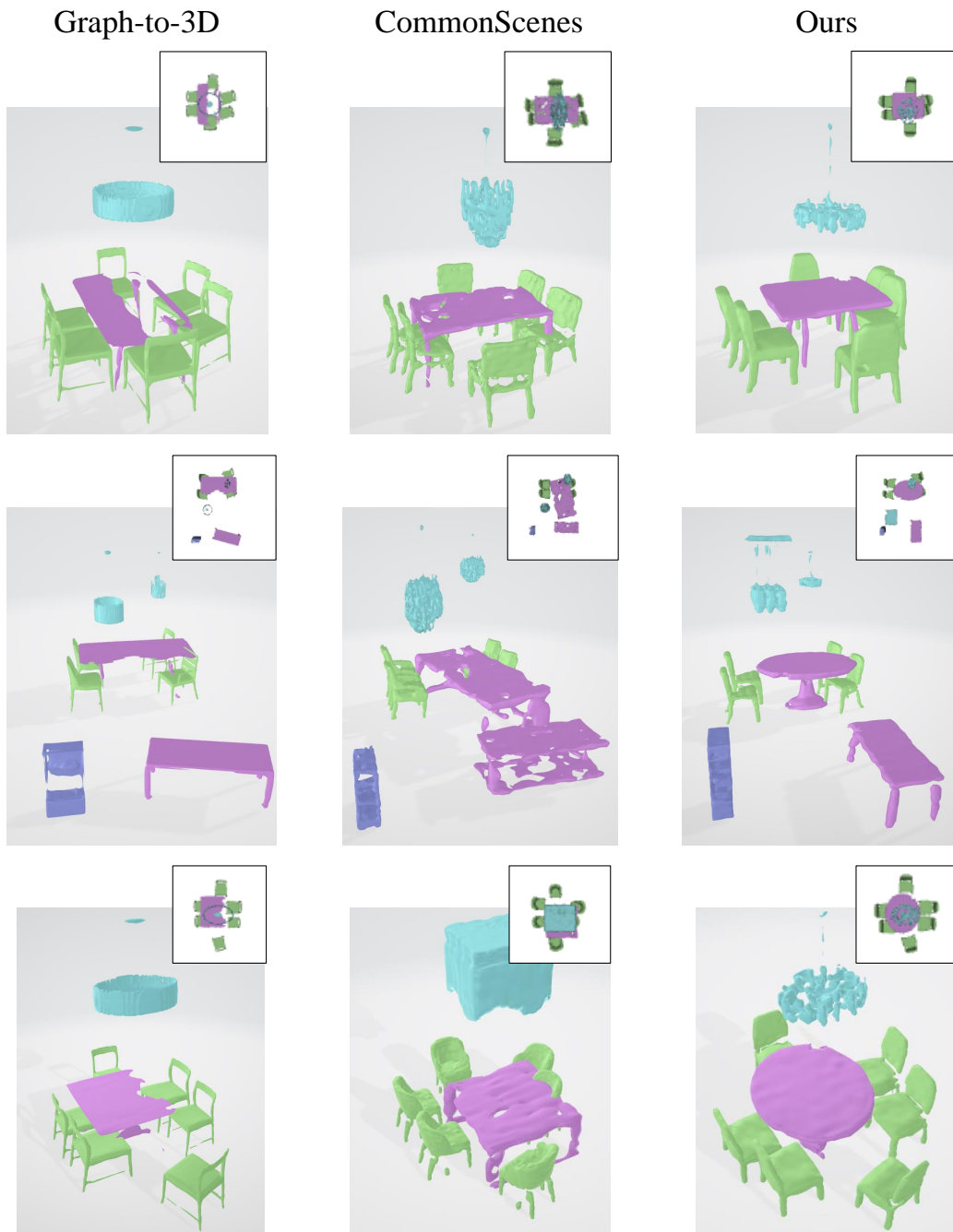


Figure 10. Additional qualitative comparisons on dining room scenes. A side view of each 3D scene is provided with a top-down view.